

# Tuning of resonance-spacing in a traveling-wave resonator device

Amir H. Atabaki\*, Babak Momeni, Ali A. Eftekhari, Ehsan S. Hosseini,  
Siva Yegnanarayanan and Ali Adibi

School of Electrical and Computer Engineering, Georgia Institute of Technology, 777 Atlantic Drive NW,  
Atlanta, GA 30332-0250, USA

\*atabaki@gatech.edu

**Abstract:** In this work a traveling-wave resonator device is proposed and experimentally demonstrated in silicon-on-insulator platform in which the spacing between its adjacent resonance modes can be tuned. This is achieved through the tuning of mutual coupling of two strongly coupled resonators. By incorporating metallic microheaters, tuning of the resonance-spacing in a range of 20% of the free-spectral-range (0.4nm) is experimentally demonstrated with 27mW power dissipation in the microheater. To the best of our knowledge this is the first demonstration of the tuning of resonance-spacing in an integrated traveling-wave-resonator. It is also numerically shown that these modes exhibit high field-enhancements which makes this device extremely useful for nonlinear optics and sensing applications.

©2010 Optical Society of America

OCIS codes: (130.3120) Integrated optics devices; (230.5750) Resonators

---

## References and links

1. R. Soref, "The Past, Present, and Future of Silicon Photonics," *IEEE J. Sel. Top. Quantum Electron.* **12**(6), 1678–1687 (2006).
  2. Q. Li, M. Soltani, S. Yegnanarayanan, and A. Adibi, "Design and demonstration of compact, wide bandwidth coupled-resonator filters on a silicon-on-insulator platform," *Opt. Express* **17**(4), 2247–2254 (2009).
  3. A. C. Turner, M. A. Foster, A. L. Gaeta, and M. Lipson, "Ultra-low power parametric frequency conversion in a silicon microring resonator," *Opt. Express* **16**(7), 4881–4887 (2008).
  4. A. M. Armani, R. P. Kulkarni, S. E. Fraser, R. C. Flagan, and K. J. Vahala, "Label-free, single-molecule detection with optical microcavities," *Science* **317**(5839), 783–787 (2007).
  5. A. H. Atabaki, M. Soltani, S. Yegnanarayanan, A. A. Eftekhari, and A. Adibi, "Optimization of Metallic Micro-Heaters for Reconfigurable Silicon Photonics," in *Conference on Lasers and Electro-Optics/International Quantum Electronics Conference*, OSA Technical Digest (CD) (Optical Society of America, 2009), paper CThB4.
  6. M. A. Popovic, T. Barwicz, F. Gan, M. S. Dahlem, C. W. Holzwarth, P. T. Rakich, H. I. Smith, E. P. Ippen, and F. X. Kärtner, "Transparent Wavelength Switching of Resonant Filters," in *Conference on Lasers and Electro-Optics/Quantum Electronics and Laser Science Conference and Photonic Applications Systems Technologies*, OSA Technical Digest Series (CD) (Optical Society of America, 2007), paper CPDA2.
  7. L. Chen, N. Sherwood-Droz, and M. Lipson, "Compact bandwidth-tunable microring resonators," *Opt. Lett.* **32**(22), 3361–3363 (2007).
  8. J. Magné, P. Giaccari, S. LaRochelle, J. Azaña, and L. R. Chen, "All-fiber comb filter with tunable free spectral range," *Opt. Lett.* **30**(16), 2062–2064 (2005).
  9. Y. G. Han, X. Y. Dong, J. H. Lee, and S. B. Lee, "Wavelength-spacing-tunable multichannel filter incorporating a sampled chirped fiber Bragg grating based on a symmetrical chirp-tuning technique without center wavelength shift," *Opt. Lett.* **31**(24), 3571–3573 (2006).
  10. M. Soltani, S. Yegnanarayanan, and A. Adibi, "Ultra-high Q planar silicon microdisk resonators for chip-scale silicon photonics," *Opt. Express* **15**(8), 4694–4704 (2007).
  11. M. Soltani, S. Yegnanarayanan, Q. Li, and A. Adibi, "Systematic Engineering of Waveguide-Resonator Coupling for Silicon Microring/Microdisk/Racetrack Resonators: Theory and Experiment," (accepted, *IEEE J. Quantum Electron.* (to appear)).
  12. H. A. Haus, *Waves and fields in optoelectronics* (Prentice-Hall, Englewood Cliffs, NJ, 1984).
  13. J. Poon, J. Scheuer, S. Mookherjea, G. Paloczi, Y. Huang, and A. Yariv, "Matrix analysis of microring coupled-resonator optical waveguides," *Opt. Express* **12**(1), 90–103 (2004).
-

## 1. Introduction

Recent technological advances in high-index-contrast material platforms, such as silicon, are promising an unprecedented level of photonics integration [1]. The development of high quality factor (Q) and compact resonators for different applications, such as, signal processing, sensing, and nonlinear optics has been an important and active area of research in this field [2–4]. Moreover, the possibility of low-power and low-loss tuning of resonance properties of such resonators has significantly enhanced device functionalities for applications where reconfiguration is required [5–7]. So far, most reconfigurable devices are envisioned for linear applications (e.g., filtering) where just one resonance mode is of interest. However, for many nonlinear optics and sensing applications, more than one wave with different frequencies may interact. To maximize the interaction of optical waves at different frequencies inside the resonator, it is essential to engineer the resonance condition at different free-spectral-ranges (FSRs), to allow the simultaneous resonance for all interacting waves. However, one of the challenges of resonance-based devices is the fixed resonance frequency spacing (or FSR) of their adjacent resonance modes which cannot be easily tuned. In many nonlinear and sensing applications, the resonance spacing is required to be trimmed after fabrication or to be dynamically tuned for higher performance [3]. The tuning of FSR has been demonstrated before in fiber-based devices [8,9]; however, there has not been any work on the tuning of the frequency spacing of adjacent resonant modes in an integrated platform. In this work we propose and experimentally demonstrate a traveling-wave resonator (TWR) structure in silicon (Si) photonics platform, in which the spacing of adjacent resonance modes can be tuned dynamically. To the best of our knowledge, this is the first demonstrating of frequency-spacing tuning in an integrated platform.

## 2. Device proposal and simulation results

TWRs are one of the more widely used types of resonators in integrated optics because of their low-loss properties [10] and easy engineering of their coupling to input/output waveguides [11]. The FSR of these resonators is given by  $\lambda^2/Ln_g$ , where  $\lambda$  is the resonance wavelength,  $L$  is the optical length of resonator, and  $n_g$  is the group index sensed by the traveling wave. Since in conventional microring, microdisk, or racetrack TWRs,  $n_g$  cannot be tuned in a wide range, FSR of these resonators is almost fixed. This very fundamental property of resonators calls for an indirect approach for the tuning of the spacing of adjacent resonant modes. In this work, we exploit the mode-splitting properties of a strongly coupled TWR device to achieve dynamic tuning of the spacing of resonant modes.

Figure 1(a) shows the structure of two identical TWRs coupled together through a general reflection-less directional coupler (DC) with power coupling coefficient  $\kappa_c^2$ . Based on the coupled-mode theory [12], it is expected that the resonance frequency of the individual resonators to split into even and odd coupled modes (or supermodes) upon coupling. The mode with lower (higher) resonance frequency is denoted as even (odd) throughout this work. This splitting can be comparable to the FSR of resonators for high enough level of coupling. Figures 1(b) and 1(c) show the two coupled-resonator structures of our interest in which coupling is achieved using one and two symmetric DCs, respectively. The power coupling coefficient of all DCs in both structures are  $\kappa^2$ . The structures in Figs. 1(b) and 1(c) are called single-point-coupled and two-point-coupled resonator structures, respectively. Figure 1(d) shows the amount of resonance-frequency splitting normalized to the FSR of each single resonator versus the power coupling coefficient of DCs (i.e.,  $\kappa^2$ ). Appendix A contains the details of the derivation of resonance condition for both devices. These simulations are performed for two identical silicon-on-insulator (SOI) coupled racetrack resonators composed of waveguides with effective refractive index and group index of 2.5 and 4.25, respectively.

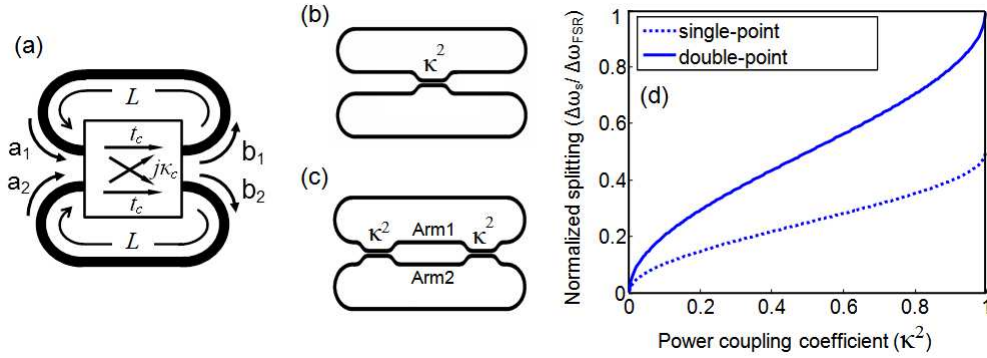


Fig. 1. (a) Structure of two identical TWRs coupled together through a general coupler: (b) and (c) show the structures of two TWRs coupled together through one and two symmetric DCs, respectively. (d) The normalized frequency splitting of the structures shown in (b) and (c) vs. power coupling coefficient.

It is observed that for single-point-coupled (Fig. 1(b)) and two-point-coupled (Fig. 1(c)) resonator structures, frequency splitting of up to half of an FSR and one whole FSR are achieved, respectively. To elucidate more, the transmission spectra of these coupled-resonator structures coupled to external bus waveguides are calculated and the results are depicted in Figs. 2(a)-2(f). The transmissions are calculated using a similar transfer-matrix approach as in Ref [13], with the transfer-matrix parameters of the single-point-coupled and two-point-coupled couplers derived in appendix A (Eqs. (5) and (6)). In these simulations an intrinsic Q of  $10^5$  is assumed for the SOI racetrack resonators with effective refractive index and group index of 2.5 and 4.25, respectively; corresponding to waveguides with a width of 480 nm and thickness of 230 nm buried under  $\text{SiO}_2$  cladding. The length of each single resonator is considered to be  $245 \mu\text{m}$  and the lower resonator is coupled to an external bus waveguide with a power coupling coefficient of  $\kappa_{ex}^2 = 0.09$ . The horizontal axes in Figs. 2(a)-2(f) is frequency detuning with respect to one of the modes of the uncoupled resonator (near  $\lambda_0 = 1.55 \mu\text{m}$ ) normalized to the FSR of the uncoupled resonator. Figures 2(a) (2(d)), 2(b) (2(e)), and 2(c) (2(f)) show the spectra for single-point-coupled (two-point-coupled) resonator structures for power coupling coefficients of  $\kappa^2 = 0$ ,  $\kappa^2 = 0.5$ , and  $\kappa^2 = 1$ , respectively. The “2x” sign next to the drops in the transmission spectra indicates the presence of two degenerate modes at that particular frequency. It is observed that as the coupling coefficient increases from zero, the initially degenerate modes split and reach their maximum splitting for  $\kappa^2 = 1$ . For the single-point-coupled structure with  $\kappa^2 = 1$ , in each round-trip, electromagnetic field from one resonator completely couples to the second resonator with the addition of a phase shift of  $\pi/2$  [12] and after traveling the second resonator, it couples back into the first resonator with an additional phase of  $\pi/2$ . As a result, the coupled-resonator device is equivalent to one resonator with twice the length of each single resonator with a total phase of  $\pi$  introduced in its roundtrip-phase. This is observed in Fig. 2(c) where the FSR of the coupled-resonator is half the FSR of each single resonator (Fig. 2(a)) and the resonances are shifted by half of an FSR because of the additional  $\pi$  phase. For the two-point-coupled structure the interference between the two arms of the balanced MZI formed between the resonators, determines the effective mutual coupling between them. For example, at  $\kappa^2 = 0.5$ , the MZI has complete power coupling between the two resonators with the addition of a  $\pi/2$  phase on the field amplitudes (excluding the propagation phase term). Hence, this structure acts exactly the same as the single-point-coupled structure with  $\kappa^2 = 1$ ; and as result, transmission spectra in Figs. 2(c) and 2(e) are the same. However, in the two-point-coupled structure, for  $\kappa^2 = 1$ , the MZI has zero power coupling between the two resonators; hence, the two resonators are decoupled with an addition of a total phase of  $\pi$  introduced in the roundtrip-phase of each resonator as a result of the MZI phase (excluding propagation phase term in the straight part of the MZI).

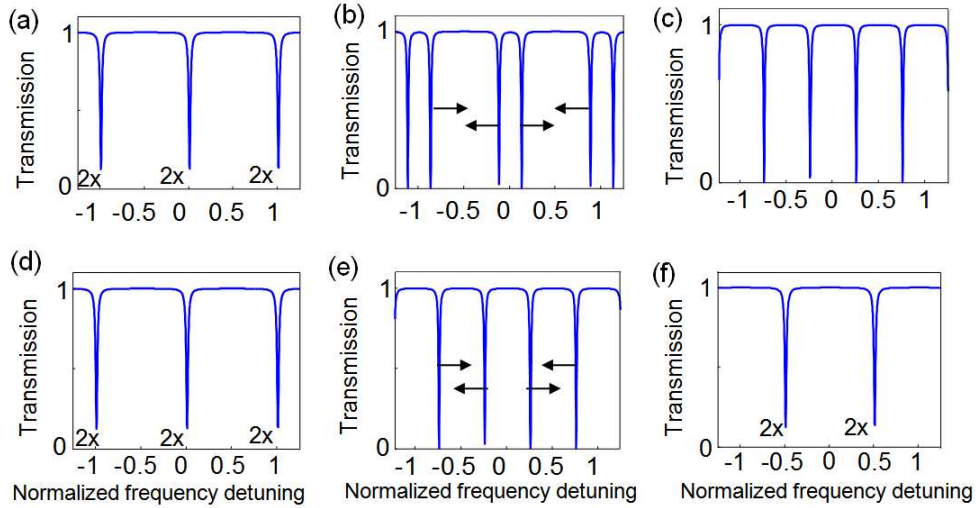


Fig. 2. (a), (b), and (c) show the transmission spectra of a single-point-coupled resonator for  $\kappa^2 = 0$ ,  $\kappa^2 = 0.5$ , and  $\kappa^2 = 1$ , respectively; coupled to an external bus waveguide. (d), (e), and (f) show the transmission spectra of a two-point-coupled resonator for  $\kappa^2 = 0$ ,  $\kappa^2 = 0.5$ , and  $\kappa^2 = 1$ , respectively. The length of each resonator is  $245 \mu\text{m}$  with an intrinsic  $Q$  is  $10^5$ .

As a result of this additional phase, the modes of the coupled-resonator structure are shifted by half of an FSR compared to the uncoupled case of  $\kappa^2 = 0$ . Therefore, by looking at the evolution of modes in Figs. 2(d) to 2(f), it is observed that as  $\kappa^2$  is increased, even and odd supermodes travel half of an FSR in opposite directions and a net splitting of one whole FSR is observed in this structure. The arrows in Figs. 2(b) and 2(e) show the direction of the shift in the resonance modes as coupling coefficients in coupling points are increased.

The two-point-coupled resonator structure not only exhibits twice as much frequency splitting compared to the single-point-coupled structure, but also has an advantage from an engineering point-of-view. The Mach-Zehnder interferometer can be utilized to tune the resonator coupling by tuning the phase difference between the two arms of the interferometer. Figure 3 shows the normalized frequency-splitting as a function of phase difference between the arms of interferometer denoted by Arm1 and Arm2 in Fig. 1(c), respectively. Since any phase change in the interferometer arms changes the resonance frequency of the corresponding resonator, the two resonators will no longer be degenerate. To investigate only the effect of the change in the mutual coupling between the resonators, in this study, the resonance frequencies of resonators are kept unchanged by adding a compensating phase term to the round-trip phase of each resonator. This phase is equal to the phase added to the MZI arm of the same resonator with an opposite sign. The power coupling coefficient,  $\kappa^2$ , used in each simulation is indicated next to the corresponding curve. It is observed that the maximum splitting occurs for zero-phase difference and as phase difference increases to  $\pi$ , coupling and therefore splitting reduces to zero. Hence, mode splitting can be tuned to reach the desired value through this mechanism.

One important characteristic of the proposed coupled-resonator device is that the amount of field enhancements in the two individual resonators changes with  $\kappa^2$  and consequently the effective length of the device changes. For example if the mutual coupling between the two resonators changes from one to zero, the effective length of the device changes from  $2L_{res}$  to  $L_{res}$ , where  $L_{res}$  is the length of each resonator. Hence, within each resonator roundtrip, the mode experiences different levels of loss as the effective coupling between the two resonators changes. However, as the coupling to the bus waveguide is fixed within each roundtrip, different levels of extinction are observed at the resonance for different coupling strengths between the resonators. This is indicative of different levels of field enhancement in the

device (e.g.: maximum enhancement is achieved at zero extinction or critical coupling condition).

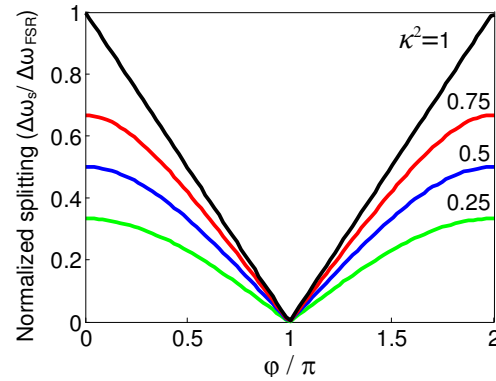


Fig. 3. Normalized frequency splitting versus the phase difference between the two arms of the interferometer coupling the two resonators in the two-point-coupled structure shown in Fig. 1(c). Numbers over the curves indicate the value of  $\kappa^2$ . In these simulations we change the phase difference between the two arms of the Mach-Zehnder resonator (Arm1 and Arm2 in Fig. 1(c)). All other parameters in these simulations are the same as those in the caption of Fig. 2.

As field enhancement is one of the more important measures in many sensing and nonlinear optics applications, the effect of resonator mutual coupling on field enhancement is studied in section 4 in detail.

### 3. Fabrication and experimental results

To experimentally demonstrate the proposed idea, the coupled-resonator device with two-point-coupling is fabricated on an SOI wafer with silicon slab thickness of 230 nm, and a 1  $\mu\text{m}$  thick buried oxide (BOX) layer (Fig. 4). Microheaters are integrated on the MZI to tune the coupling between the resonators. The width of the waveguides throughout the device is 480 nm to assure single-mode operation. The length of each resonator is 245  $\mu\text{m}$  (including MZI length) and each arm of the Mach-Zehnder interferometer is 60  $\mu\text{m}$  long. The DCs are identical and the gap and length of the parallel coupling region is 150 nm and 7.5  $\mu\text{m}$ , respectively. The pattern of the device is written on ZEP electron-beam resist using electron-beam lithography (JEOL 9300) and etched in silicon by inductively-coupled-plasma (STS ICP) using a  $\text{Cl}_2$ -based chemistry. After this step, 1  $\mu\text{m}$   $\text{SiO}_2$  is deposited using plasma-enhanced chemical-vapor-deposition (PECVD) and microheater patterns are defined by a lift-off process using ZEP and electron-beam evaporation. Optimized microheaters with rapid reconfiguration have been developed to achieve sub-microsecond reconfiguration [5]. Microheaters are composed of 75 nm thick nickel and contact pads are covered with 150 nm gold for better electrical contact. Single-step lift-off of both nickel and gold is performed at the locations of the heaters and contact pads. In another lithography step, areas over microheaters are opened using ZEP resist, and gold is removed using nickel-safe GE-8148 gold etchant (Transene Inc.).

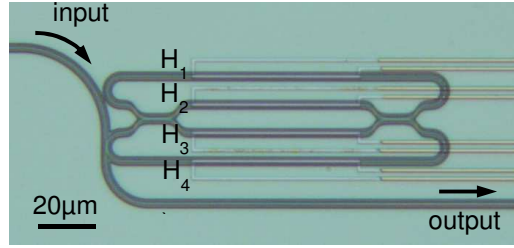


Fig. 4. Optical micrograph of the two-point-coupled resonator structure fabricated on SOI with integrated microheaters.  $H_1$ ,  $H_2$ ,  $H_3$ , and  $H_4$  show the microheaters fabricated on top of the structure for thermal tuning.

Figure 4 shows the optical micrograph of the photonic device with integrated microheaters. Separate heaters are allocated to different parts of the device for independent control over coupling and resonance wavelength.

The transmission is measured by coupling light into and out of the device using tapered fibers in a standard optical characterization test setup. The TE-polarized light is incident on the device from a swept-wavelength tunable laser and the output of the device is coupled into a photodetector and the data is transferred to the PC using a data-acquisition (DAQ) card. Figure 5(a) shows the transmission spectrum of the device shown in Fig. 4. It is observed that two sets of modes with similar FSR of about 2.3 nm are present in the spectrum. This FSR corresponds to the FSR of each single resonator (which is 2.3 nm). Also, the spacing between two adjacent modes from different sets corresponds to the mode splitting of the otherwise degenerate modes of the resonators. Because of the high level of coupling, modes of the two resonators are strongly split by approximately 0.86 nm. From this amount of splitting, power coupling coefficient of each DC between the two resonators is calculated to be  $\kappa^2 = 0.42$ , assuming the two couplers are identical. Intrinsic Q of the modes of the coupled-resonator structure is also measured to be 70,000.

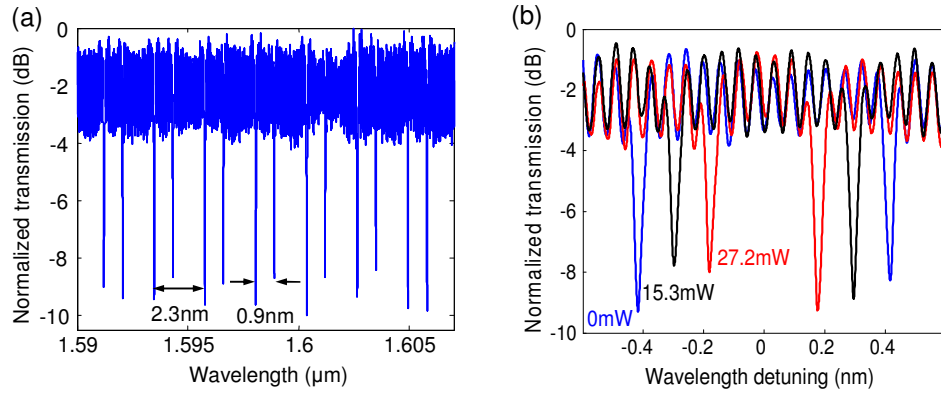


Fig. 5. (a) Normalized transmission spectrum of the coupled resonator structure shown in Fig. 4. (b) Normalized transmission spectra of the two coupled modes near  $\lambda = 1.601 \mu\text{m}$  for different power dissipations in heater  $H_2$  (Fig. 4). Horizontal axis is wavelength detuning with respect to the center of the two coupled modes. A wavelength offset is added to the data to compensate for the red-shift in the resonance wavelengths of the modes in the coupled-resonator structure.

By heating the upper interferometer arm through heater  $H_2$  (Fig. 4), coupling between the two resonators can be tuned. Figure 5(b) depicts the normalized transmission spectra of the two coupled resonance modes in the vicinity of  $\lambda = 1.601 \mu\text{m}$  for three different levels of power dissipation in heater  $H_2$ . The number next to each spectrum is the power dissipation in the microheater. Similar tuning results are obtained for other FSRs in Fig. 5(a). Horizontal



axis in Fig. 5(b) shows the wavelength detuning from the center of the coupled modes (or supermodes). It is observed that as the phase mismatch between the arms of the interferometer is increased (through applying heat), coupling between the resonators and consequently the mode spacing between the coupled modes is decreased. In addition to the change in the resonator coupling strengths, resonance wavelength of the upper resonator is red-shifted while heating the upper interferometer arm. This causes the center of the two coupled resonant modes (even and odd supermodes) to be red-shifted as their spacing is reduced. Here, this red-shift is compensated by introducing an appropriate wavelength offset to the experimental data, so that the centers of coupled-modes in each transmission spectrum match. In practice, by simultaneous tuning of all fabricated heaters, center wavelength of two resonators can remain unchanged while their mutual coupling is tuned. Figure 6 shows the change in resonance wavelength spacing of the even and odd coupled-modes for the structure in Fig. 4 for different power dissipations in heater  $H_2$ . It is observed that 0.4 nm change in wavelength spacing between coupled modes is achieved by dissipating 27 mW in  $H_2$ . This amount of change is equivalent to 20% of the FSR of the uncoupled resonators.

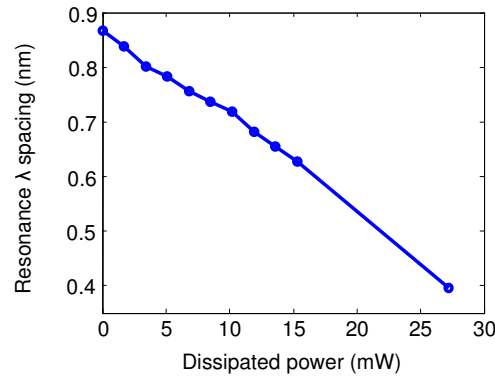


Fig. 6. Resonance wavelength spacing versus power dissipation in heater  $H_2$  for the structure shown in Fig. 4.

#### 4. Discussion

The results shown in Section 3 clearly show that the spacing of the adjacent modes of the resonator-based device can be tuned by a relatively large amount by using a single heater. The fact that the splitting between adjacent modes in Fig. 4 can change from 0.86 nm (zero power dissipation) to 0.4 nm (equal to 20% of an FSR) with only 27 mW heating power dissipation in  $H_2$ , proves that the resonator-based device in Fig. 4 can be used for a large set of signal conditions in applications like nonlinear optics in which signals with different wavelengths interact. By tuning the mode spacing, we can achieve resonance condition and simultaneous field enhancement for the involved signals. The amount of field-enhancement is an important characteristic which determines the device performance and needs to be addressed for any proposed device. As our proposed resonator structure is composed of an interferometer in addition to resonators, its field-enhancement characteristic is expected to be different compared to a simple resonator. Using a similar transfer-matrix approach as in Ref [13], field-enhancement of the even and odd supermodes in the two resonators of the two-point-coupled structure (Fig. 1(c)) are calculated as a function of phase difference between the two arms of the interferometer, and the results are shown in Fig. 7. In these simulations, the total lengths of both resonators are 245  $\mu\text{m}$ ; the lengths of the interferometer arms are 60  $\mu\text{m}$ ; the power coupling coefficients of DCs between the two resonators are  $\kappa^2 = 0.7$ ; and the power coupling coefficient for the coupling of the bus waveguide to the lower resonator is  $\kappa_{ex}^2 = 0.09$  (close to the critical coupling condition for an intrinsic Q of  $10^5$ ). The intensity enhancements shown in Fig. 7 are denoted by  $a$  and defined by the ratio of the intensity of the field of each resonant mode inside the resonator to the intensity of the field at the input waveguide. Subscripts 1 and

2 determine the fields in the bottom resonator ( $R_1$ ) and the top resonator ( $R_2$ ), respectively. Also, the modes with lower and higher frequency are called even and odd mode, respectively. Figure 7 shows that as the MZI phase difference increases, the amount of enhancement of the even (odd) mode in  $R_1$  increases (decreases) until  $\varphi = 0.8\pi$ . As  $\varphi$  further increases,  $R_2$  becomes decoupled from  $R_1$ ; the field in  $R_2$  drops to zero; and the enhancement of both even and odd modes increases in  $R_1$ . The reason for this high increase in the field-enhancement is because of the decrease in the effective length of the coupled-resonator system as the resonators are decoupled. This decrease in the effective length results in the decrease of the mode-volume of the structure, which directly translates into a higher field enhancement. In simulations, as  $\varphi$  approaches  $\pi$ , even and odd modes gradually overlap and become numerically indistinguishable. In Fig. 7, the dashed lines connect the last simulation point for which even and odd modes were distinguishable (i.e.,  $\varphi = 0.95\pi$ ) to the limiting case of zero coupling (i.e.,  $\varphi = \pi$ ), where the two modes completely overlap. It is observed that in each resonator ( $R_1$  and  $R_2$ ) both even and odd modes exhibit field enhancement simultaneously. This confirms that waves in resonance with these modes exhibit enhanced nonlinear interaction. However, this enhancement varies as the resonance frequency spacing is tuned and this has to be taken into account for any application.

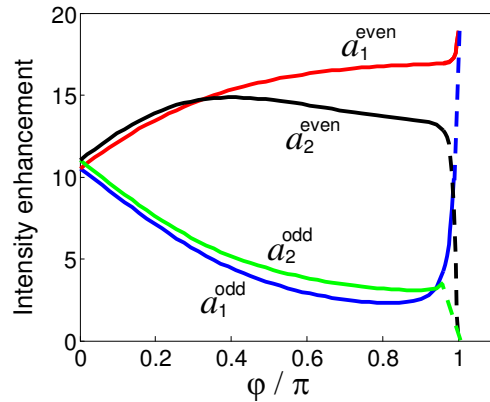


Fig. 7. Intensity enhancement of even and odd supermodes in  $R_1$  (bottom resonator) and  $R_2$  (top resonator) as a function of the phase difference between the interferometer arms in Fig. 1(c). Dashed parts of each curve connects the last simulation data-point for which the odd and even modes could be resolved, to the final value at  $\pi$  phase-shift (uncoupled case).

## 5. Conclusion

In conclusion, we have theoretically and experimentally demonstrated a coupled-resonator device in which the spacing between its adjacent modes can be tuned through tuning of their mutual coupling. The device was fabricated on an SOI platform with integrated microheaters for the purpose of tuning. By over-coupling the two resonators, a mode splitting as high as 0.86 nm (0.374xFSR) is achieved and this splitting was tuned down to 0.4 nm by heating one arm of the interferometer coupling the two resonators. To the best of our knowledge this is the first demonstration of a resonator-based device in an integrated platform in which the spacing between the adjacent resonance modes is tuned by 20% of its FSR. Through numerical simulations we have also shown that both of the split supermodes exhibit high field enhancements, which is the requirement for nonlinear optics and sensing applications.

## Appendix A. Resonance condition of the coupled-resonator device

Here, we derive the resonance condition of the device shown in Fig. 1(a) using the transfer-matrix method [13]. If we assume that the vectors  $\vec{a} = [a_2 \ a_1]^T$  and  $\vec{b} = [b_2 \ b_1]^T$  in Fig. 1(a) represent the wave amplitudes entering and exiting the DC, respectively; we have [12]



$$\bar{b} = \mathbf{T}\bar{a} = e^{-j\theta_c} \begin{bmatrix} t_c & j\kappa_c \\ j\kappa_c^* & t_c^* \end{bmatrix} \bar{a} , \quad (1)$$

where  $\mathbf{T}$  is the transfer matrix of a general DC coupling the two resonators in which  $\theta_c$  is the propagation phase, and  $t_c$  and  $\kappa_c$  are the amplitude through and cross-coupling coefficients, respectively. Also, through the feedback path from  $\bar{b}$  to  $\bar{a}$  we have

$$\bar{a} = e^{-j\beta L} \bar{b} , \quad (2)$$

where  $L$  is the length of each resonator and  $\beta$  is propagation constant of resonators. By combining Eqs. (1) and (2) we have

$$|\mathbf{T} - e^{j\beta L} \mathbf{I}| = 0 , \quad (3)$$

and by substituting for  $\mathbf{T}$  from Eq. (1) in Eq. (3), the following eigenvalue equation for the resonance frequency of the coupled-resonator device is derived:

$$e^{j2\phi} + 2\text{Re}\{t_c\}e^{j\phi} + 1 = 0 . \quad (4)$$

Here,  $\phi = \theta_c + \beta L$  and  $\text{Re}\{.\}$  represents the real part of the argument in the parentheses. It should be noted that since very strong coupling between resonators is considered, first-order coupled-mode-theory could not be used here [2].

Figures 1(b) and 1(c) show the two coupled-resonator structures of our interest in which coupling is achieved using one and two symmetric DCs, respectively. The power through and coupling coefficients of all DCs in both structures are denoted by  $t^2$  and  $\kappa^2$ , respectively. For the coupler in the single-point-coupled resonator (Fig. 1(b)), we have

$$t_c = t, \quad \kappa_c = k, \quad \theta_c = 0, \quad (5)$$

and for the MZI coupler in the two-point-coupled resonator (Fig. 1(c)), we have,

$$t_c = t^2 e^{-j\Delta\phi_{MZ}/2} - k^2 e^{j\Delta\phi_{MZ}/2}, \quad \kappa_c = 2kt \cos(\Delta\phi_{MZ}/2), \quad \theta_c = \phi_{MZ}^{ave}, \quad (6)$$

where,  $\Delta\phi^{MZ} = \phi_1^{MZ} - \phi_2^{MZ}$  and  $\phi_{ave}^{MZ} = (\phi_1^{MZ} + \phi_2^{MZ})/2$ ; where,  $\phi_1^{MZ}$  and  $\phi_2^{MZ}$  are the propagation phase terms in Arm1 and Arm2 of the Mach-Zehnder, respectively. By substituting Eqs. (5) and (6) into Eq. (3) and by solving the eigenvalue equation, resonance frequencies of the coupled-resonator structures and consequently, their resonance splitting are calculated and shown in Fig. 1(d).

### Acknowledgments

This work was supported by Air Force Office of Scientific Research under Contract No. FA9550-07-1-0201 (G. Pomrenke).